Pressure-Induced Amorphization in Single-Crystal Ta_2O_5 Nanowires: A Kinetic Mechanism and Improved Electrical Conductivity

Xujie Lü,[*,†,‡] Qingyang Hu,[§] Wenge Yang,[*,‡] Ligang Bai,[†] Howard Sheng,[§] Lin Wang,[‡] Fuqiang Huang,[∥] Jianguo Wen,[⊥] Dean J. Miller,[⊥] and Yusheng Zhao[*,†]

[†]High Pressure Science and Engineering Center, University of Nevada, Las Vegas, Nevada 89154, United States

[‡]High Pressure Synergetic Consortium, Geophysical Laboratory, Carnegie Institution of Washington, Argonne, Illinois 60439, United States
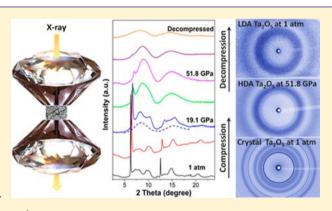
[§]School of Physics, Astronomy, and Computational Sciences, George Mason University, Fairfax, Virginia 22030, United States

[∥]CAS Key Laboratory of Materials for Energy Conversion, Shanghai Institute of Ceramics, Chinese Academy of Sciences (CAS), Shanghai 200050, People's Republic of China

[⊥]Electron Microscopy Center, Argonne National Laboratory, Argonne, Illinois 60439, United States

S *Supporting Information*

ABSTRACT: Pressure-induced amorphization (PIA) in single-crystal Ta_2O_5 nanowires is observed at 19 GPa, and the obtained amorphous Ta_2O_5 nanowires show significant improvement in electrical conductivity. The phase transition process is unveiled by monitoring structural evolution with *in situ* synchrotron X-ray diffraction, pair distribution function, Raman spectroscopy, and transmission electron microscopy. The first principles calculations reveal the phonon modes softening during compression at particular bonds, and the analysis on the electron localization function also shows bond strength weakening at the same positions. On the basis of the experimental and theoretical results, a kinetic PIA mechanism is proposed and demonstrated systematically that amorphization is initiated by the disruption of connectivity between polyhedra (TaO_6 octahedra or TaO_7 bipyramids) at the particular weak-bonding positions along the *a* axis in the unit cell. The one-dimensional morphology is well-preserved for the pressure-induced amorphous Ta_2O_5, and the electrical conductivity is improved by an order of magnitude compared to traditional amorphous forms. Such pressure-induced amorphous nanomaterials with unique properties surpassing those in either crystalline or conventional amorphous phases hold great promise for numerous applications in the future.

INTRODUCTION

Pressure-induced amorphization (PIA) has drawn great attention because of its fundamental importance in the fields of physics, chemistry, and materials and earth sciences.[1−3] It is also considered as a powerful way to synthesize new amorphous materials that can be structurally different from traditional amorphous forms.[4−6] The pressure-induced amorphous phase is a kinetically preferred state arising because of frustration of the crystalline state upon reaching high-pressure equilibrium.[7] PIA was first observed in ice (H_2O) and later discovered in several other materials, especially in tetrahedrally coordinated materials, such as Si and SiO_2,[1,8−10] while PIA in some materials (e.g., TiO_2 and Y_2O_3) was only observed when the particle size is below a critical value or in nanostructured forms.[11−15] From the application point of view, the key purposes of high-pressure studies are aimed at discovering new high-pressure phases with novel properties and understanding phase transition mechanisms.[16] As is well-known, properties of materials can be modified by tailoring either chemical composition or microstructure. If a high-pressure phase can be preserved at ambient conditions, its novel properties could be retained, which provides a new pathway to design materials with tailored properties. To date, few studies have reported the improved properties of materials after amorphization and there is still a wide spectrum of opinions on the PIA mechanism. Herein, we report the PIA in crystalline tantalum oxide (Ta_2O_5) nanowires and the improved performance of the obtained amorphous Ta_2O_5.

Ta_2O_5 is an important wide-band gap semiconductor ($E_g = 4$ eV). With the high dielectric constant, high refractive index, outstanding photoelectric properties, and high chemical stability, Ta_2O_5 has been widely used in dynamic random access memory devices, capacitor, atomic switch, antireflective coating layer, gas sensor, photocatalysis, etc.[17−22] At ambient pressure, Ta_2O_5 undergoes a phase transformation above 1590

K from a low-temperature orthorhombic phase (L-Ta_2O_5) to a high-temperature phase (H-Ta_2O_5) with several different variants (monoclinic, orthorhombic, and tetragonal cells).[23,24] Because of the complex crystal structure of Ta_2O_5, some other polymorphs have been reported. The TT-Ta_2O_5 (analogue of TT-Nb_2O_5) and T-Ta_2O_5 were synthesized by Hummel et al.[25] The ε-Ta_2O_5 polymorph was reported by Izumi et al. using a hydrothermal method at 570−620 K.[26] Besides the crystalline phases, amorphous Ta_2O_5 (a-Ta_2O_5) is also an important technological material. As reported, a-Ta_2O_5 possesses valuable properties for applications because of its isotropic characters. For instance, in the application of dynamic random access memories, a-Ta_2O_5 has better leakage current characteristics than the crystalline phase, while the crystalline phase has a higher dielectric constant.[27,28] The pressure-induced amorphous phase derived from the crystalline phase is structurally different from the traditional amorphous phase: it is amorphous but retains some microclusters from its crystalline parent.[7] Thus, it can be expected that pressure-induced amorphous materials may possess some advantageous properties from both amorphous and crystalline phases.

Orthorhombic Ta_2O_5 can be considered as a quasi-octahedrally coordinated material, which is built up of edge- and corner-shared TaO_6 octahedra and TaO_7 pentagonal bipyramids.[29,30] It is expected to be a good candidate for studying PIA and the mechanism because of its peculiar structure of elongated unit cell in one direction (a axis). Thus far, there is still no report on PIA in this system. In this paper, we provide direct evidence of PIA in single-crystal Ta_2O_5 nanowires using *in situ* synchrotron X-ray diffraction (XRD), pair distribution function (PDF), Raman spectroscopy, and transmission electron microscopy (TEM). We investigated the PIA mechanism on the basis of local structure evolution within a unit cell under high pressure, and a kinetic mechanism is proposed and well-demonstrated by both experimental and calculated results. High-pressure resistance measurements were carried out to explore the electrical conductivity evolution during the compression−decompression cycle. This study provides not only a new window for experimental and theoretical understanding of amorphization under high pressure but also a synthetic guideline for high-performance amorphous nanomaterials from their crystalline phases.

■ RESULTS AND DISCUSSION

The structure and morphology of the pristine crystalline Ta_2O_5 nanowires were characterized by XRD, scanning electron microscopy (SEM), and TEM. As shown in Figure S1 of the Supporting Information, the individual nanowire is a single crystal with about 30 nm in diameter and several micrometers in length. The powder XRD pattern consists of mostly broad and three sharp peaks (at 2θ positions of 6.28°, 12.56°, and 18.87°), which can be indexed to the orthorhombic Ta_2O_5 phase (PDF 79-1375) with a space group of $Pmm2$ and lattice constants of a = 43.997 Å, b = 3.894 Å, and c = 6.209 Å.[25] The three sharp peaks can be assigned to (010), (020), and (030) in sequence, corresponding to the preferential growth of the nanowire along the b axis. The broad peaks are caused by the nanosized effect, and the adjacent peaks merge together with each other. The selected area electron diffraction (SAED) pattern of an individual nanowire confirms that it is single-crystalline and grows along the [010] direction.

Ta_2O_5 nanowires were loaded in a symmetrical diamond anvil cell with neon as a pressure transmitting medium for *in*

situ high-pressure study (see the Experimental Section for details). Synchrotron XRD patterns of Ta_2O_5 nanowires were collected at different pressures during compression and decompression. Figure 1a shows the unrolled two-dimensional
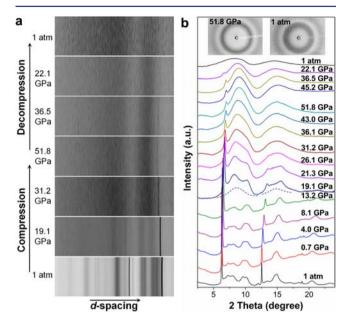

Figure 1. Synchrotron XRD data of Ta_2O_5 nanowires obtained during compression and decompression. PIA takes place at about 19 GPa, and the amorphous phase remains after decompressing to ambient conditions. (a) Unrolled 2D XRD images and (b) integrated XRD patterns. Dashed lines indicate contribution from the amorphous phase. The insets in panel b show the 2D XRD images of the sample under 51.8 GPa and after decompression.

(2D) XRD images at seven selected pressures, and Figure 1b shows the integrated one-dimensional (1D) XRD profiles. With the increase of the pressure, all diffraction peaks shift to larger 2θ values, the peak intensities weaken, and the peak widths broaden gradually. When the applied pressure exceeds 19 GPa, structural disorder sets in, as evidenced by the appearance of new broad peaks (indicated by dashed lines in Figure 1b) that represent the contributions from the amorphous phase and the gradual disappearance of other diffraction peaks, which indicates the onset of partial amorphization. As the pressure further increases to 36 GPa, all of the diffraction peaks disappear except for the (010) peak, and two broad peaks associated with an amorphous phase are observed obviously at about 8.5° and 14.5°. The weak (010) peak remains with the highest pressure of 51.8 GPa in this study.

During decompression, the amorphous structure synthesized by PIA is retained to ambient pressure. It is interesting to note that the remaining (010) peak weakens gradually during decompression and totally disappears as the pressure was released to ambient. This observation implies that, in the high-pressure amorphous phase, even though the overall crystalline structure is heavily disordered, some small clusters retain local periodicity along the crystalline b axis. This partially local ordered high-pressure amorphous phase loses its stability when the pressure is fully released. The broadening of the peaks from the amorphous phase during decompression is related to changes in medium-range ordering. The significantly broadened peaks after total pressure release indicate a much looser structure in the final amorphous phase. The insets in Figure 1b

show the original 2D diffraction images of the sample at the highest pressure of 51.8 GPa (left) and after decompression (right), which indicate different local structure between the high-pressure a-Ta_2O_5 and the recovered amorphous phase. XRD results reveal the irreversibility of PIA in Ta_2O_5 nanowires, and this provides a new method for synthesizing the amorphous nanomaterials.

The PIA in Ta_2O_5 nanowires was also observed with the *in situ* high-pressure Raman spectroscopy study. Figure 2 shows
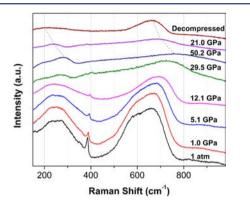

Figure 2. Raman spectra of Ta_2O_5 nanowires measured during compression and decompression. The excitation laser wavelength is 514.5 nm.

the Raman spectra of Ta_2O_5 nanowires measured during compression and decompression. One sharp peak at 386 cm^{-1} and several broad peaks at 225, 274, 591, 665, and 822 cm^{-1} are observed at ambient conditions. As reported, the Raman bands between 100 and 450 cm^{-1} are associated with O−Ta−O bending modes in TaO_6 octahedra, while those between 450 and 900 cm^{-1} mainly correspond to the various Ta−O stretching modes associated with edge-shared polyhedra.[31−33] The Raman results from our sample are similar to those reported in the literature.[32,34] The broadened and shifted bands are caused by the low-dimension and nanosize effect of the Ta_2O_5 nanowires. With the increase of the pressure, all Raman peaks have a blue shift, as expected for pressure-induced bond shortening, and their intensities weaken gradually. The spectra from 29.5 GPa and above are largely different from those at lower pressures, indicating that the amorphous phase takes the dominant role at these pressures. At 50.2 GPa, only two broad peaks can be observed even with a much longer acquisition time. For the decompressed sample, it also shows two broad peaks but significantly different from the high-pressure amorphous form. All of these features are in good agreement with the XRD results and confirm the occurrence of PIA in Ta_2O_5 nanowires.

To reveal the morphology and structure change of Ta_2O_5 nanowires during amorphization, we carried out TEM and high-resolution transmission electron microscopy (HRTEM) analysis of the pristine sample and the samples decompressed from 19.2 and 51.8 GPa. For the sample released from 51.8 GPa, the local structure of the as-prepared a-Ta_2O_5 can be observed, and we expected to see the structure of Ta_2O_5 nanowires at the beginning stage of amorphization in the sample released from 19.2 GPa. The bright-field and HRTEM images are shown in Figure S3 of the Supporting Information and Figure 3. From Figure S3 of the Supporting Information, one can see that the 1D nanowire morphology is well-preserved after amorphization. In the HRTEM image of a-Ta_2O_5
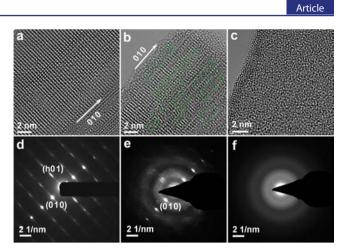

Figure 3. HRTEM images and SAED patterns of Ta_2O_5 nanowires from (a and d) pristine sample and recovered samples from (b and e) 19.2 GPa and (c and f) 51.8 GPa, respectively.

recovered from 51.8 GPa (Figure 3c), no crystalline lattice is observed and the structure is totally disordered. For the sample decompressed from 19.2 GPa, some amorphous segments appeared within the crystalline lattice (Figure 3b and Figure S3d of the Supporting Information), which contribute to the two broad amorphous peaks in the XRD pattern. The coexistence of amorphous, crystal phases and the intermediate state in the sample recovered from 19.2 GPa was further confirmed by the fast Fourier transform (FFT) from the selected HRTEM regions (see Figure S4 of the Supporting Information).

A PIA mechanism based on the melting curve of a material was proposed, in which a system with potential for PIA and polyamorphic transition has a melting curve with a negative Clapeyron slope ($−dT_m = dP$) or the appearance of maxima in the melting curve.[35] This thermodynamic mechanism has been used to explain the transition in H_2O, Si, and SiO_2, but we cannot yet test this proposition for Ta_2O_5. Herein, we focus on the local structural process of amorphization and the influence of the crystal structure on the phase transitions in this system.

The crystal structure of orthorhombic Ta_2O_5 provides insight into the structural stability and pressure-induced phase transition mechanism. In a unit cell of orthorhombic Ta_2O_5, the polyhedra are connected in pairs, with one corner (sharing one oxygen atom) along the b axis, with a total of 25 shared corners (Figure 4a). Similarly, the polyhedra are connected with each other by many corners or edges (sharing two oxygen atoms), along the a and c axes (Figure 4b). The space between polyhedra is more easily compressed than the polyhedra themselves. From the mechanical-stability point of view, breaking the connection of polyhedra in the a axis is much easier than that in the b and c axes. As a particular example, around the circled regions in Figure 4b, the large spaces are relatively easier to compress and would be the weaker connections under pressure. Therefore, the coherence along the [100] direction may break first at the critical pressure, resulting in either amorphization or transition to a high-pressure crystalline phase with a new unit cell. Considering the nanosize effect in our Ta_2O_5 nanowire system, the PIA would be preferred, which can be triggered by enlarging G_d to enable $G_a < G_c + G_d$, where G_a, G_c, and G_d are the free energies of the amorphous phase, the metastable crystalline phase, and the defects under high pressure, respectively.[11,13]
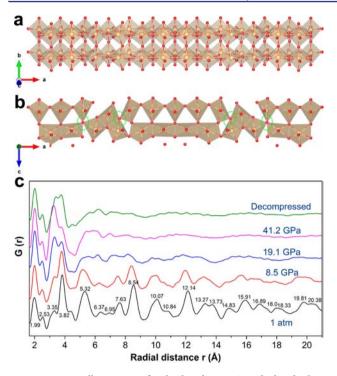
Figure 4. Unit-cell structure of orthorhombic Ta_2O_5, which is built up of edge- and corner-shared TaO_6 octahedra and TaO_7 pentagonal bipyramids: viewing along (a) c axis and (b) b axis. (c) PDF patterns of Ta_2O_5 nanowires under compression and after the pressure was released.

highlighted regions in Figure 5a, electrons are most localized to anions (Figure 5b), indicating the ionic bonding nature. The
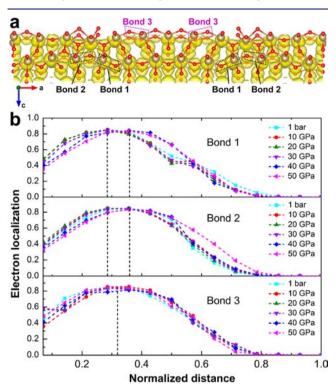

Figure 5. ELF analysis for the Ta_2O_5 unit cell. (a) ELF distribution in space. The isosurfaces are taken as ELF = 0.58. (b) ELF profiles for the Ta–O bonds in three different fenced regions. Dashed lines indicate the most localized section along the Ta–O bonds.

To simulate the amorphization process in theory, we carried out the first principles calculations on the evolutions of both phonon modes and electron localization function (ELF) under pressure. By perturbing the relaxed unit cell using a finite difference method, the dynamical matrix can be determined and diagonalized to obtain the phonon modes. In Figure S5 of the Supporting Information, our simulated vibrational frequency spectra show the O–Ta–O bending modes $(100-400~cm^{-1})$ and the Ta–O stretching modes $(450-600~cm^{-1})$ softening during compression. The bending modes around $230~cm^{-1}$ at ambient pressure are mostly associated with the TaO_6 polyhedrons near the two end regions along the $[100]$ direction in the Ta_2O_5 unit cell (as marked in Figure 4b). Those modes, along with the stretching modes, show a blue shift with increasing pressure because of the bond shortening. Above 30 GPa, an obvious bending mode softening was observed and all mode peaks continuously broadened upon further compression. The simulated results well-reproduced our experimental observations (Raman spectra). From our *ab initio* geometric relaxation results, such mode softening could induce bond breakage and recoordination at those particular positions, resulting in the phase transition to smaller subunit cells along the a axis. Because only one unit cell was used in simulation, the nanosize effects and the generation of defects were not thoroughly considered. In experiments, such effects could largely influence the crystallization process of the metastable phase. PIA observed in experiments can be explained by a lack of sufficient thermal energy at room temperature in the Ta_2O_5 nanowire system.

Bonding strength is signified by the sharing and localization of valence electrons between bonding atoms, which can be reflected by the so-called ELF (see the Experimental Section for details).[36,37] Overlaying the ELF profiles of atom pairs in the

connections of polyhedra around bonds 1 and 2 have only four shared corners along the a axis and are more likely to be broken under pressure because of the weaker linking and larger vacancy spaces. Bond 2 belongs to the regions in which O–Ta–O bending modes become soft during compression (see Figure S5 of the Supporting Information). An obvious shift of electron localization to cations was observed above 30 GPa in both bonds 1 and 2, indicating the weakening of the bond strength, whereas the most localization section for bond 3 did not show any shift of electron localization during compression. The weakening of bonds near two end sections of the $[100]$ direction in the unit cell (bonds 1 and 2) reconfirmed our assumption that amorphization would first occur at those weak bonding regions in the a axis.

Combining the calculation results and TEM data, we proposed that the amorphization was induced by the disruption of connectivity between the polyhedra at particular bonds in the a axis because the move of these polyhedra under pressure is easier and faster than others. At the beginning stage of amorphization, the connection between the polyhedra collapsed first at the weak bonding positions along the a axis in the Ta_2O_5 unit cell. This can be further proven by comparing the SAED patterns of a single nanowire before compression and that released from 19.2 GPa (panels d and e of Figure 3). From Figure 3e, we can see that the amorphous rings appeared and the diffraction spots corresponding to (h01) became very indistinct or disappeared but that of (010) was still clear and sharp. It should be pointed out that the diffraction spots of (h01) originating from low-index planes (close to the center)

disappeared, indicating the collapse of the unit cell along the [100] direction. We can also find the collapses directly in the HRTEM image, as marked by rectangles in Figure 3b, in which it is seen that the atomic arrangements are not in periodic format anymore and the amorphous structure has formed instead. As the pressure further increased, the amorphous area expanded to cover the entire space at around 50 GPa. Because we noticed that there is a weak (010) peak remaining in the XRD pattern even at the highest pressure, we consider that some small clusters still have local periodicity along the [010] direction under high pressure. This can be explained because the movement of the atoms is constrained by the pressure, while that constraint is gradually released during decompression, resulting in the decrease of the (010) peak intensity. Eventually, the structure became totally amorphous at ambient pressure (panels c and f of Figure 3). The morphology of the nanowires remains after the pressure-induced phase transitions, which means that the 1D amorphous Ta_2O_5 nanomaterial can be synthesized by high-pressure treatment.

To demonstrate the process described above and further understand local structure evolution during amorphization, high-pressure PDF measurement was carried out using high-energy XRD. The PDF results are shown in Figure 4c. The position of each peak represents the distance between each pair of atoms. The first sharp peak at 1.99 Å and the shoulder peak at 2.53 Å are assigned to the nearest Ta−O and O−O bonds in each polyhedron, respectively. The shifts of Ta−O and O−O peaks under pressure are very small, which indicates that such bonds are rigid and the polyhedra themselves are hard to compress. The peaks at 3.35 and 3.82 Å originate from the Ta−Ta bonds between the nearest edge-shared polyhedra and the nearest corner-shared polyhedra, respectively. The rest of the well-resolved peaks arise from the various Ta−Ta bonds. By counting the various Ta−Ta bond distances and comparing to PDF spectra, we conclude that the peaks assigned to Ta−Ta bonds crossing the weak bonding points (as circled in Figure 4b and bonds 1 and 2 in Figure 5a) with long distances decreased quickly under pressure and disappeared at the amorphization point of 19 GPa, such as peaks at 13.27, 13.75, 14.83, 15.91, 16.89, 18.33, 19.81, and 20.38 Å, while the peaks attributed to Ta−Ta bonds within each subparts still existed at the beginning stage of amorphization (see detailed analysis and discussion in the Supporting Information). This observation confirms our proposed PIA mechanism that the connectivity between polyhedra along the [100] direction broke down first at the weak-bonding positions under pressure and then triggered the amorphization. When pressure increased to 41.2 GPa, only the peaks representing the bonds within each polyhedron and the nearest corner- or edge-shared polyhedra remain, indicating the disappearance of long-range order and the formation of the amorphous structure.

It is worth noting that the peak at 3.82 Å (Ta−Ta bonds between the nearest corner-shared polyhedra) weakens gradually and the peak at 3.35 Å (Ta−Ta bonds between the nearest edge-shared polyhedra) increases with pressure; particularly at the amorphization point of 19 GPa, the 3.35 Å peak became stronger than the 3.82 Å peak. It suggests that corner-shared polyhedra were changing into an edge-shared configuration during amorphization and the edge-shared polyhedra with higher density are preferred for the amorphous phase under high pressure. Upon the pressure released, the intensity of such two peaks reversed, which may suggest the existence of polyamorphism in Ta_2O_5 nanowires and the

transition from a high-density amorphous (HDA) form to a low-density amorphous (LDA) form during decompression.

The electrical conductivity of Ta_2O_5 is very important for many applications, such as photovoltaic devices and gas sensors. To explore the conductivity evolution, we carried out *in situ* resistance measurement in diamond anvil cell (DAC) during compression and decompression. The resistance was calculated by the Van de Pauw method using the equation $\exp(-\pi R_1/R_S) + \exp(-\pi R_2/R_S) = 1$, where R_1 and R_2 are the two resistances measured by the four-probe method (see details in the Supporting Information) and R_S is the sheet resistance of the sample.[38] Figure 6a shows the resistance change with the
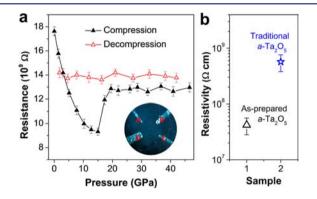

Figure 6. (a) Resistances of Ta_2O_5 nanowires versus pressure during compression and decompression. Solid and open symbols represent compression and decompression procedures, respectively. (b) Resistivity comparison of traditional and pressure-induced a-Ta_2O_5. The inset in panel a displays a microphotograph of the Ta_2O_5 sample in DAC with four Pt probes.

increase and decrease of the pressure. At first ($P < 3$ GPa), the resistance decreased with an increasing pressure because the contact between the nanowires is better under compression. As the pressure further increases, intimate contact between the nanowires has been achieved and the resistance from the material itself becomes dominant. The pressure-induced resistance drop at this stage is often associated with the broadening and eventual overlap of the valence and conduction bands, caused by the shortening and bending of bonds.[39,40] A precipitous increase of the resistance between 15 and 17 GPa can be observed, which is caused by the occurrence of PIA in the sample at this pressure. Many defects that arose from amorphization act as the scattering centers for electron transport to increase resistance. The pressure for amorphization deduced from the resistance measurements (15−17 GPa) is somewhat lower than that determined from XRD (19−21 GPa). The deviation in transition pressure is probably due to the different hydrostatic conditions because the resistance measurement was conducted without any pressure-transmitting medium. As reported, non-hydrostatic pressure leads to shear stress and asymmetrical distortion, accelerating the growth of disorder and, thus, lowering the PIA pressure.[41]

During further compression to 50 GPa and subsequent decompression to ambient pressure, there is no obvious change in resistance. This is interesting because, in general, the resistance should increase with the development of disorder and the reduction of crystallinity. The abnormal phenomenon may be caused by the special structure of the pressure-induced amorphous form; it is amorphous but inherits some local structures from its parent crystalline phase.[7] The results reveal

that the pressure-induced amorphous Ta_2O_5 nanowires have better conductivity than expected. The electrical resistivity was estimated to be 4.2×10^7 Ω cm using the sheet thickness of 30 μm. For comparison, we measured the resistivity of traditional amorphous Ta_2O_5 powders, which is more than an order of magnitude higher than that of the as-prepared a-Ta_2O_5 (5.7×10^8 versus 4.2×10^7 Ω cm, as shown in Figure 6b). In addition, other studies even reported higher resistivity values from other forms of amorphous Ta_2O_5 ($>10^{10}$ Ω cm).[42−44] Therefore, the pressure-induced a-Ta_2O_5 nanomaterial with improved electron transport ability appears to be a promising functional material in many energy-related applications, such as photovoltaic devices.

■ CONCLUSION

In summary, our studies demonstrate the PIA in single-crystal Ta_2O_5 nanowires by high-pressure XRD, PDF, Raman spectra, and TEM analysis. The PIA-produced amorphous Ta_2O_5 can be recovered to ambient pressure, and the 1D morphology of Ta_2O_5 nanowires is well-preserved after amorphization. A new kinetic mechanism of PIA is proposed that the amorphization is associated with the disruption of connectivity between polyhedra (octahedra or bipyramids) at particular positions in the a axis because of the relatively weaker bonding. The pressure-induced local structure evolution within a unit cell is systematically investigated by both *in situ* experiments and first principles calculations, and the proposed mechanism is further evidenced by PDF and TEM observations. The electrical transport measurements reveal an order of magnitude improvement in conductivity of pressure-induced amorphous Ta_2O_5 nanowires compared to the traditional amorphous Ta_2O_5 materials. The results show that PIA is a useful method for synthesizing new amorphous materials expecting to possess the advantages of both amorphous and crystalline phases and also provide a new perspective for understanding the PIA mechanism, which would guide us to discover more pressure-induced amorphous materials with improved properties.

■ EXPERIMENTAL SECTION

Sample Preparation. The synthesis of Ta_2O_5 nanowires has been described in detail in previous work.[21] Briefly, Ta_2O_5 powder (99.85%, Alfa Aesar) was first dissolved in hydrofluoric acid solution and reprecipitated by adding ammonia solution. Then, the freshly formed precipitate was redissolved in a solution containing hydrogen peroxide and ammonia (5:1 by volume) to obtain a precursor and transferred to a Teflon-lined autoclave reacting at 240 °C for 24 h. Finally, the resultant product was washed thoroughly with deionized water and ethanol and freeze-dried overnight prior to being characterized.

In Situ **High-Pressure Characterizations.** A symmetric DAC was used to generate high pressure. A rhenium gasket was pre-indented to 30 μm in thickness, and then a hole with a diameter of 120 μm was laser-drilled to serve as the sample chamber. A pre-compressed Ta_2O_5 power pallet and a small ruby ball were loaded in the chamber. Neon was used as the pressure-transmitting medium, and the pressure was determined by the ruby luminescence method.[45] The high-pressure angle-dispersive X-ray diffraction (ADXD) experiments were carried out at the 16 BM-D station of High-Pressure Collaborative Access Team (HPCAT), Advanced Phonon Source (APS), Argonne National Laboratory (ANL). A focused monochromatic beam with about 5 μm in diameter [full width at half maximum (fwhm)] and wavelength of 0.4246 Å was used for the diffraction experiments. High-pressure Raman spectra were measured in DAC with neon as the pressure-transmitting medium by a Raman spectrometer with a 514.5 nm laser excitation. Data suitable for PDF analysis were collected at the 11 ID-B station at APS in ANL, using high-energy X-ray (90.42 keV; λ =

0.1370 Å) in combination with a large amorphous silicon-based area detector. The 2D scattering images were integrated into 1D data within fit2d. The PDFs, $G(r)$, were extracted within PDFgetX2, subtracting contributions from the background and Compton scattering to the total scattering data.[46]

Microstructure Observations. A scanning electron microscope (JEOL JSM-6700F) and field-emission transmission electron microscopes (FEI Titan 80-300ST TEM/STEM, with a CEOS spherical and chromatic aberration imaging corrector, and JEOL JEM 2100F, working at 200 kV) were used to investigate the morphology and detailed structure of the pristine and high-pressure recovered samples. In this work, after decompression from pressures of 19.2 and 51.8 GPa, we opened the DACs, transferred the samples from the chamber to clean glass slides with a tiny pin, and then dropped a little ethanol on the samples to disperse the materials onto holey carbon grids with a Cu support.

High-Pressure Resistance Measurement. Electrical resistance was measured by a four-probe resistance test system in a DAC at pressures up to 50 GPa. A boron nitride (BN) layer was inserted between the Re gasket and diamond culet to provide electrical insulation between the electrical leads and metal gasket. Four platinum leads (2 μm thick) were arranged to contact the sample in the chamber (see Figure S7 of the Supporting Information). A Keithley 6221 current source, 2182A nanovoltmeter, and 7001 switch system were used as the current supply, voltmeter, and voltage/current switcher, respectively. The resistance was determined by the Van de Pauw method (see details in the Supporting Information).[38]

First Principles Calculations. The calculations are implemented with the projector augmented wave (PAW) method in the framework of density functional theory (DFT) through Vienna *ab initio* simulation package.[47,48] For tantalum atoms, 5p and 6s electrons were treated as free electrons. Only 2s and 2p electrons of oxygen atoms were considered as valence states. A plane-wave basis set with a kinetic energy cut off of 550 eV is employed to set up the wave functions in the core regions. Generalized gradient approximation under Perdew−Wang parametrization is chosen for the exchange correlation functionals.[49] The results reported in this paper were carried out on a single Ta_2O_5 nanowire unit cell. The Brillouin zone is sampled by a mesh of $1 \times 9 \times 9$ k points using the tetrahedron integration method, providing 41 irreducible k points. Hydrostatic pressure is applied by adding pulay stress to the diagonal elements of the stress tensor. At each pressure, the unit cell is optimized for atomic position, cell shape, and cell volume until the force acting on each atom is less than 0.01 eV/Å.

The electron localization can be reflected by the ELF[36,37]

$$ ELF = \frac{1}{1 + (D_\sigma/D_\sigma^0)^2} $$

where D_σ is a measure of Pauli replusion and scales with the probability to find a neighboring same-spin electron. D_σ^0 is a normalization factor determined by a D_σ that is in a homogeneous electron gas having the same level of spin density. ELF thus ranged from 0 (no localization) to 1 (perfect localization), and ELF = 0.5 represents the case of homogeneous electron gas. A higher value of ELF indicates that the electrons are more localized. In our simulation, ELF values are calculated on the same grid as the charge density. The bonding atoms are connected by a fictitious tube that was divided into 14 sections. The ELF values on each section are then averaged and profiled to the Ta−O bonds (Figure 5b).

■ ASSOCIATED CONTENT

⑤ Supporting Information

Details of the pair distribution function analysis, four-probe resistance measurement, characterizations of pristine Ta_2O_5 nanowires, Raman spectra, XRD patterns decompressed from a maximum pressure of 19.2 GPa, TEM images of Ta_2O_5 nanowires decompressed from 51.8 and 19.2 GPa, FFT patterns from three selected areas of the HRTEM image,

phonon mode calculation results, and statistical analysis of bond distances in the orthorhombic Ta_2O_5 unit cell. This material is available free of charge via the Internet at http://pubs.acs.org.

■ AUTHOR INFORMATION

Corresponding Authors
xujie@aps.anl.gov
wyang@ciw.edu
yusheng.zhao@unlv.edu

Notes
The authors declare no competing financial interest.

■ ACKNOWLEDGMENTS

■ REFERENCES

(1) Mishima, O.; Calvert, L. D.; Whalley, E. *Nature* **1984**, *310*, 393.
(2) Deb, S. K.; Wilding, M.; Somayazulu, M.; McMillan, P. F. *Nature* **2001**, *414*, 528.
(3) Perottoni, C. A.; de Jornada, J. A. H. *Science* **1998**, *280*, 886.
(4) Kruger, M. B.; Jeanloz, R. *Science* **1990**, *249*, 647.
(5) Mukherjee, G. D.; Vaidya, S. N.; Sugandhi, V. *Phys. Rev. Lett.* **2001**, *87*, 195501.
(6) Kawai, N.; Atou, T.; Ito, S.; Yubuta, K.; Kikuchi, M.; Nakamura, K. G.; Kondo, K. *Adv. Mater.* **2007**, *19*, 2375.
(7) Sharma, S. M.; Sikka, S. K. *Prog. Mater. Sci.* **1996**, *40*, 1.
(8) Hemley, R. J.; Jephcoat, A. P.; Mao, H. K.; Ming, L. C.; Manghnani, M. H. *Nature* **1988**, *334*, 52.
(9) Tse, J. S.; Klug, D. D. *Phys. Rev. Lett.* **1993**, *70*, 174.
(10) Zhang, J.; Zhao, Y.; Xu, H.; Zelinskas, M. V.; Wang, L.; Wang, Y.; Uchida, T. *Chem. Mater.* **2005**, *17*, 2817.
(11) Swamy, V.; Kuznetsov, A.; Dubrovinsky, L. S.; McMillan, P. F.; Prakapenka, V. B.; Shen, G.; Muddle, B. C. *Phys. Rev. Lett.* **2006**, *96*, 135702.
(12) Li, Q.; Liu, B.; Wang, L.; Li, D.; Liu, R.; Zou, B.; Cui, T.; Zou, G.; Meng, Y.; Mao, H. K.; Liu, Z.; Liu, J.; Li, J. *J. Phys. Chem. Lett.* **2010**, *1*, 309.
(13) Wang, L.; Yang, W.; Ding, Y.; Ren, Y.; Xiao, S.; Liu, B.; Sinogeikin, S. V.; Meng, Y.; Gosztola, D. J.; Shen, G.; Hemley, R. J.; Mao, W. L.; Mao, H. K. *Phys. Rev. Lett.* **2010**, *105*, 095701.
(14) Machon, D.; Daniel, M.; Bouvier, P.; Daniele, S.; Le Floch, S.; Melinon, P.; Pischedda, V. *J. Phys. Chem. C* **2011**, *115*, 22286.

(15) Piot, L.; Le Floch, S.; Cornier, T.; Daniele, S.; Machon, D. *J. Phys. Chem. C* **2013**, *117*, 11133.
(16) Wang, Z.; Wen, X. D.; Hoffmann, R.; Son, J. S.; Li, R.; Fang, C. C.; Smilgies, D. M.; Hyeon, T. *Proc. Natl. Acad. Sci. U.S.A.* **2010**, *107*, 17119.
(17) Ezhilvalavan, S.; Tseng, T. *J. Mater. Sci.* **1999**, *10*, 9.
(18) Sreethawong, T.; Ngamsinlapasathian, S.; Suzuki, Y.; Yoshikawa, S. *J. Mol. Catal. A: Chem.* **2005**, *235*, 1.
(19) Sakamoto, T.; Lister, K.; Banno, N.; Hasegawa, T.; Terabe, K.; Aono, M. *Appl. Phys. Lett.* **2007**, *91*, 092110.
(20) Gu, T.; Tada, T.; Watanabe, S. *ACS Nano* **2010**, *4*, 6477.
(21) Lu, X.; Ding, S.; Lin, T.; Mou, X.; Hong, Z.; Huang, F. *Dalton Trans.* **2012**, *41*, 622.
(22) Osada, M.; Sasaki, T. *Adv. Mater.* **2012**, *24*, 210.
(23) Lagergren, S.; Magnéli, A. *Acta Chem. Scand.* **1952**, *6*, 444.
(24) Liu, X. Q.; Han, X. D.; Zhang, Z.; Ji, L. F.; Jiang, Y. J. *Acta Mater.* **2007**, *55*, 2385.
(25) Hummel, H. U.; Fackler, R.; Remmert, P. *Chem. Ber.* **1992**, *125*, 551.
(26) Izumi, F.; Kodama, H. *J. Less-Common Met.* **1979**, *63*, 305.
(27) Chaneliere, C.; Four, S.; Autran, J. L.; Devine, R. A. B.; Sandler, N. P. *J. Appl. Phys.* **1998**, *83*, 4823.
(28) Nakagawa, Y.; Okada, T. *J. Appl. Phys.* **1990**, *68*, 556.
(29) Stephenson, N. C.; Roth, R. S. *Acta Crystallogr., Sect. B: Struct. Crystallogr. Cryst. Chem.* **1971**, *27*, 1037.
(30) Stephenson, N. C.; Roth, R. S. *J. Solid State Chem.* **1971**, *3*, 145.
(31) Dobal, P. S.; Katiyar, R. S.; Jiang, Y.; Guo, R.; Bhalla, A. S. *J. Appl. Phys.* **2000**, *87*, 8688.
(32) Dobal, P. S.; Katiyar, R. S.; Jiang, Y.; Guo, R.; Bhalla, A. S. *Int. J. Inorg. Mater.* **2001**, *3*, 135.
(33) Chen, Y.; Fierro, J. L. G.; Tanaka, T.; Wachs, I. E. *J. Phys. Chem. B* **2003**, *107*, 5243.
(34) Dobal, P. S.; Katiyar, R. S.; Jiang, Y.; Guo, R.; Bhalla, A. S. *J. Raman Spectrosc.* **2000**, *31*, 1061.
(35) Richet, P.; Gillet, P. *Eur. J. Mineral.* **1997**, *9*, 907.
(36) Becke, A. D.; Edgecombe, K. E. *J. Phys. Chem.* **1990**, *92*, 5397.
(37) Silvi, B.; Savin, A. *Nature* **1994**, *371*, 683.
(38) van der Pauw, L. J. *Philips Res. Rep.* **1958**, *13*, 1.
(39) Ma, Y.; Eremets, M.; Oganov, A. R.; Xie, Y.; Trojan, I.; Medvedev, S.; Lyakhov, A. O.; Valle, M.; Prakapenka, V. *Nature* **2009**, *458*, 182.
(40) Arai, K.; Kumata, K.; Kadota, K.; Yamamoto, K.; Namikawa, H.; Saito, S. *J. Non-Cryst. Solids* **1973**, *13*, 131.
(41) Goncharov, A. F. *High Pressure Res.* **1992**, *8*, 607.
(42) Young, P. L. *J. Appl. Phys.* **1976**, *47*, 235.
(43) Liu, J.; Wei, A.; Zhao, X.; Zhang, H. *Bull. Mater. Sci.* **2011**, *34*, 443.
(44) Flannery, W. E.; Pollack, S. R. *J. Appl. Phys.* **1966**, *37*, 4417.
(45) Mao, H. K.; Xu, J.; Bell, P. M. *J. Geophys. Res.* **1986**, *91*, 4673.
(46) Wiaderek, K. M.; Borkiewicz, O. J.; Castillo-Martínez, E.; Robert, R.; Pereira, N.; Amatucci, G. G.; Grey, C. P.; Chupas, P. J.; Chapman, K. W. *J. Am. Chem. Soc.* **2013**, *135*, 4070.
(47) Kresse, G.; Joubert, D. *Phys. Rev. B: Condens. Matter Mater. Phys.* **1999**, *59*, 1758.
(48) Kresse, G.; Furthmüller, J. *Comput. Mater. Sci.* **1996**, *6*, 15.
(49) Perdew, J. P.; Wang, Y. *Phys. Rev. B: Condens. Matter Mater. Phys.* **1992**, *45*, 13244.